Guohao Hu
State Key Laboratory of High Temperature Gas Dynamics, Institute of Mechanics, Chinese Academy of Sciences, Beijing 100190, China; School of Engineering Science, University of Chinese Academy of Sciences, Beijing 100049, China
e-mail: huguohao@imech.ac.cn

Fengquan Zhong[1]
State Key Laboratory of High Temperature Gas Dynamics, Institute of Mechanics, Chinese Academy of Sciences, Beijing 100190, China; School of Engineering Science, University of Chinese Academy of Sciences, Beijing 100049, China
e-mail: fzhong@imech.ac.cn

Mengmeng Du
State Key Laboratory of High Temperature Gas Dynamics, Institute of Mechanics, Chinese Academy of Sciences, Beijing 100190, China; School of Engineering Science, University of Chinese Academy of Sciences, Beijing 100049, China
e-mail: 1412857929@qq.com

Qinyang Wang
Beijing Aerospace Technology Institute, Beijing 100074, China
e-mail: 907052276@qq.com

Honglin Kang
Beijing Aerospace Technology Institute, Beijing 100074, China
e-mail: klgiant@163.com

Coupled Heat Transfer Properties of Aluminum/Titanium Alloy Plates With Kerosene Active Cooling

Active cooling is an effective thermal protection method for plates under high thermal loading. In this paper, characteristics of coupled heat transfer of aluminum alloy and titanium alloy plates with kerosene active cooling are studied numerically and experimentally. The effects of cooling channel spacing as well as the inlet parameters of kerosene on the maximum temperature and temperature uniformity of the plate are investigated with varied heat fluxes. Besides, the thermal resistance and flow resistance of kerosene cooling are also analyzed. The experimental results show that the 2a12-type aluminum alloy plate can be cooled to a maximum temperature of 460 K with kerosene cooling under a mass flowrate of 24.7 g/s and heat flux of 6–11 kW/m^2. The numerical results show that the maximum temperature is mainly affected by the channel spacing and heat flux. Compared to the titanium alloy plate, the aluminum alloy plate is more likely to be affected by the coolant mass flowrate. In addition, the conductive thermal resistance of aluminum alloy plates is 0.0017–0.0079 m^2 K/W and is 0.015–0.073 m^2 K/W for titanium alloy plates. For both materials, conductive thermal resistance dominates the total thermal resistance of plates with active cooling. [DOI: 10.1115/1.4054009]

Keywords: thermal protection, active cooling, thermal resistance, aerospace heat transfer

1 Introduction

Active cooling is an effective way for the thermal protection of hot plates for engineering applications. Different from passive cooling based on the thermal shielding mechanism of coating materials, coolant is introduced to channels and absorbs heat from hot plates for an active cooling methodology. The overall cooling efficiency can be controlled and optimized via coolant mass flowrate and geometrical parameters of cooling channels. Meanwhile, with active cooling, the volume and the weight of the structure can be reduced significantly. Therefore, active cooling has been widely used in aero-engine [1–8] and photovoltaic (PV) [9,10] applications due to its superiority of high efficiency. Li et al. [11] studied a double-layer cooling structure using *n*-decane as a coolant under a 1.5 MW/m^2 heat flux condition. The numerical results show that when flow directions of coolant are the same in the double-layer cooling structure, the cooling performance is better and heat transfer deterioration is effectively weakened. Wang et al. [12] tested heat transfer and flow characteristics of supercritical kerosene in square and circular channels with ribbed roughness. The experimental results show that the ribbed roughness can improve the heat transfer performance while the pressure drop is increased. Dang et al. [13] studied heat transfer deterioration of kerosene flow in a circular pipe by the Reynolds-averaged Navier–Stokes (RANS) numerical method. Their results show that the heat transfer deterioration attributes to the decrease of turbulence intensity in the vicinity of the pipe wall. Jing et al. [14] developed a self-adaptive method of fuel distribution in cooling channels by using a mini-structure. The results show that mini-structure can improve the mass flow uniformity between parallel channels and obviously improve the overall cooling performance. Xu et al. [15] numerically studied flow and heat transfer characteristics of low-temperature methane in a ribbed tube with a wall heat flux of 1.0–4.0 MW/m^2. The results show that the ribbed tube surface has a significant enhancement effect on heat transfer performance.

Researches about the heat transfer performance of coolant flow have been studied sufficiently, and the effect of coolant and channel parameters is reported by many scholars. However, the coupling effect of heat transfers of solid structure and coolant flow is rarely studied. It is well known that aluminum alloy (2a12) and titanium alloy (TA15) are widely used as skin materials for aircraft and automotive industries [16,17] due to their relatively

[1]Corresponding author.

Manuscript received December 1, 2021; final manuscript received February 17, 2022; published online April 6, 2022. Assoc. Editor: Qiang Zhang.

low density and good mechanical properties. 2a12 has a low softening tendency at high temperatures and can serve at temperatures lower than 500 K. TA15 has good thermal stability and strength, and it can work for a long time at a temperature less than 773 K. However, for higher working temperature, aluminum and titanium alloys cannot serve stably for a long time. Extra thermal protection such as active cooling is required. Heat transfer properties of alloy plates with active cooling are necessary to be studied.

In this paper, coupled heat transfer of 2a12 and TA15 plates with kerosene cooling effect is studied numerically and experimentally. The effects of cooling channel spacing, kerosene mass flowrate, and the loaded heat flux on the maximum temperature and temperature uniformity of alloy plates are numerically studied. In addition, thermal resistance and flow resistance are analyzed for varied plate structures and cooling conditions.

2 Experimental Study

2.1 Experimental Setup. The schematic of the experimental setup is shown in Fig. 1. The heat transfer facility includes four subsystems: (1) fuel driven and control system, (2) test section with radiant heating equipment, (3) water-cooling and fuel collection system, and (4) measurement and data acquisition system. Before the experiment, fuel tanks are filled with RP-3 kerosene, and the test plate is preheated via quartz lamp heating to a preset temperature. The kerosene is then driven by high-pressure nitrogen gas, and its mass flowrate is measured by a volumetric flowmeter (accuracy ±1%). As kerosene flows through the cooling channel, the alloy plate gradually reaches a thermal steady state under a combination effect of radiant heating and kerosene cooling. At the outlet of the cooling channel, the heated kerosene flows into a water-cooling tank to be cooled down and then collected. During the experiments, temperatures on the plate surface and in the cooling channel as well as the pressure difference between the inlet and the outlet of the channel are measured and used for further analysis of flow and heat transfer properties. After the test, the quartz lamp heating is turned off, and nitrogen is blown into the cooling channel and pipe loop to clean the residual kerosene and to cool the test plate and pipe system.

2.2 Test Plates and Data Measurements. An aluminum alloy plate with a cooling structure is tested experimentally. Figure 2 shows a schematic diagram of the test plate with dimensions. The plate is 400 mm long and 210 mm wide and has a thickness of 3 mm. Cutting technology is used to machine the plate with a rectangular cooling structure of 11×11 mm^2. The diameter of the circular cooling channel is 5 mm. The physical parameters of 2a12 and TA15 are, respectively, shown in Tables 1 and 2 according to the literature [18]. Photographs showing the test plate installed in the heating facility are shown in Figure 3.

A quartz lamp array is installed above the test plate and used to generate heating. The bottom surface of the plate structure is insulated. The heat fluxes at different streamwise and spanwise locations are measured by heat flux sensor (accuracy 3%), and the measurement result is shown in Fig. 4(*a*). Inverse-distance interpolation is used to calculate the total heat flux distribution in the experimental section, as shown in Fig. 4(*b*). The absorption ratio of the aluminum alloy surface is 22.5%. Ten type-K thermocouples with an accuracy of ±2 K are spot-welded on the bottom surface of the plate, in which the T11–T15 thermocouples are evenly spaced along the streamwise x-direction and at a spanwise position of $y =$ 52.5 mm, and the T21–T25 thermocouples are evenly spaced along the x-direction and located at a spanwise position of $y =$ 157.5 mm. Four type-K sheath thermocouples with a diameter of 1.0 mm are installed in the cooling channel for fluid temperature measurement and their locations are shown in Fig. 2. A thin-film sputtering pressure sensor with an accuracy of 1% is used to measure the pressure of the coolant. A high-accuracy differential pressure gauge with an accuracy of ±0.15% is used to measure the pressure difference between the channel inlet and outlet.

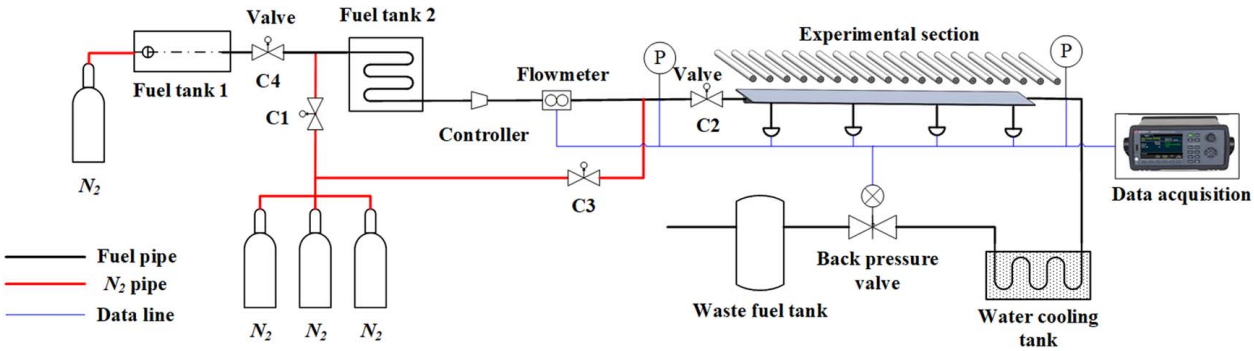

Fig. 1 Schematic diagram of the experimental setup

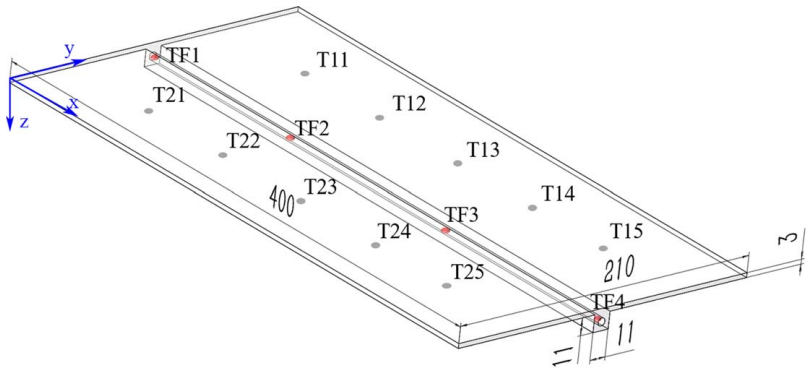

Fig. 2 Schematic diagram of the 2a12 plate with cooling structure

Table 1 Thermal properties of 2a12 material [18]

T (K)	373	473	573
c_p (J/(kg K))	921	1047	1130
λ (W/(m K))	130	147	163

Table 2 Thermal properties of TA15 material [18]

T (K)	373	473	573	673	773	873
c_p (J/(kg K))	545	587	628	670	712	755
Λ (W/(m K))	8.8	10.2	10.9	12.2	13.8	15.1

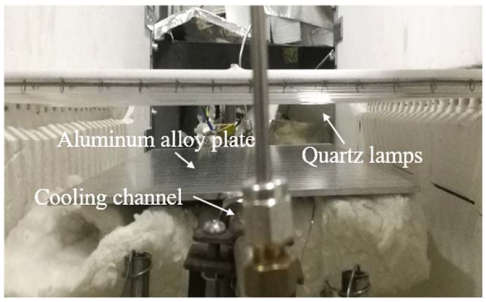

Fig. 3 The test plate installed below the quartz lamp array

2.3 Experimental Conditions. Two tests for aluminum alloy plates are conducted. The main experimental parameters are shown in Table 3.

2.4 Experimental Results and Discussions. The time change of the wall and fuel temperatures is shown in Fig. 5(*a*). During the period of the first 140 s, the plate is heated by quartz lamps and the wall temperatures of T11–T25 always increase with time. In this stage, the kerosene temperatures of TF11–TF14 also rise since the fuel thermocouples installed in the cooling channel are heated as well. From $t = 154$ s, kerosene begins to flow through the cooling channel and the wall temperatures increase with much smaller rates and then gradually approach constants. At the same time, the kerosene temperatures also reach equilibrium states. After kerosene cooling of 46 s, the heating system is turned off and nitrogen is blown to clean the residual fuel in the channel

Table 3 Experimental conditions

Case	$\dot{m}$ (g/s)	T_{in} (K)	Pressure (MPa)	Power (kW)	Material
Case A1	24.7	291.2	3.0	5.3	2a12
Case A2	34.7	290.4	3.0	5.6	2a12

and pipe system. From Fig. 5(*a*), it is obvious that the wall temperatures would keep rising without the cooling effect. With kerosene cooling, the wall temperatures at different locations are finally stabilized in the range of 432–455 K.

Figures 5(*b*)–5(*d*) show the time development of mass flowrate and the outlet pressure of kerosene as well as the pressure drop through the cooling channel. It is obvious that all the parameters reach a steady state at approximately $t = 160$ s when kerosene starts to flow into the cooling channel for about 6 s. It can be seen from Fig. 5 that the mass flowrate and the pressures are stable during the heating period of $t = 160$ s to $t = 205$ s and fluctuations of mass flowrate and pressures are negligible.

The wall temperatures of Case A1 at equilibrium state are plotted as a function of streamwise distance and shown in Fig. 6(*a*). Two groups of wall temperatures indicated by different symbols are located symmetrically on two sides of the plate and are marked by T11–T15 and T21–T25 as indicated in Fig. 2. It is found that the wall temperature is higher in the plate middle part, which is partly caused by the heat flux distribution generated by the quartz lamp array. The two temperature groups are very close to each other indicating a good symmetry in the spanwise direction. Figure 6(*b*) shows the measured fuel temperature along the channel axis. The fuel temperature increases almost linearly and the temperature rise of 13 K is found.

Figures 7(*a*) and 7(*b*) show the wall and fuel temperatures for Case A2. The temperature distributions are quite similar to that of Case A1. In both Figs. 6 and 7, the calculated temperature distributions are also plotted, and the details of the numerical method are addressed in the following section.

3 Numerical Study

3.1 Computational Domain and Boundary Conditions. The coupled heat transfer of alloy plate and kerosene coolant flow is numerically studied via solid–fluid heat coupling calculation. The physical properties of 2a12 and TA15 are shown in Tables 1 and 2, and the 10-species surrogate model was used to determine the thermophysical properties of RP-3 kerosene [19]. The numerical

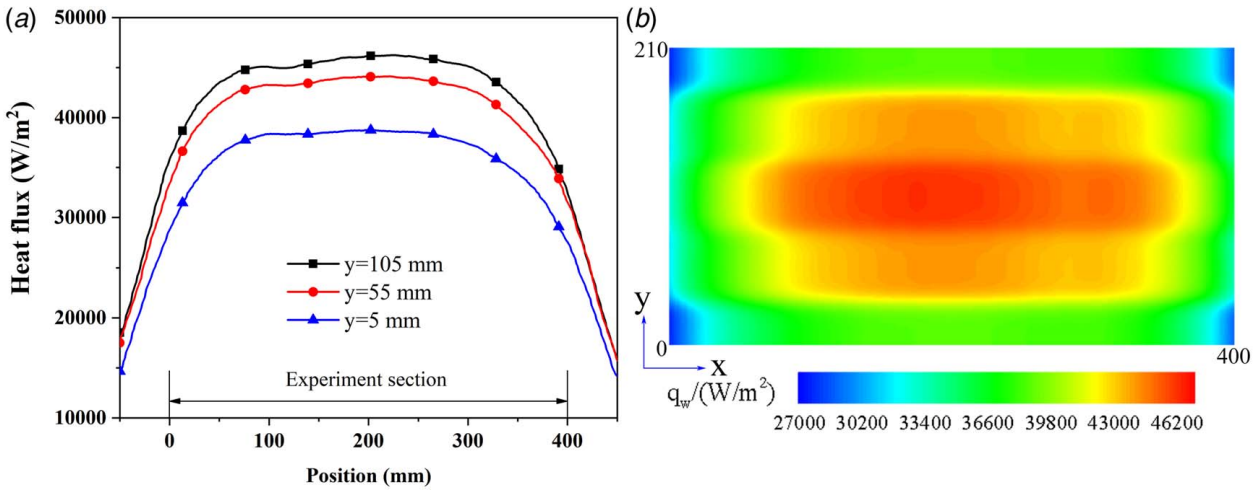

Fig. 4 The total heat flux of Case A1: (*a*) measurement result and (*b*) inverse-distance interpolation distribution

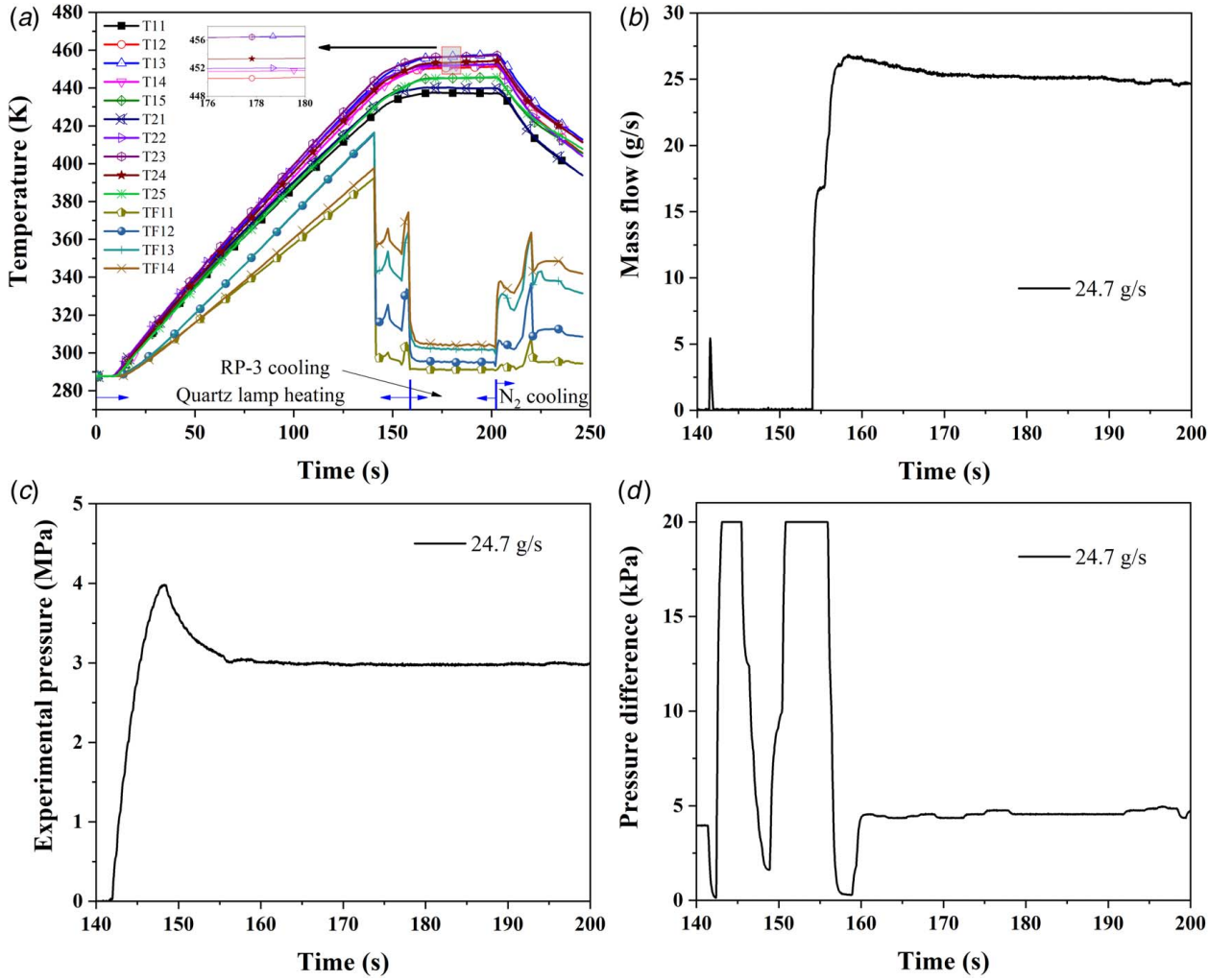

Fig. 5 Time development of temperatures and pressures for test Case A1: (*a*) temperature, (*b*) mass flow, (*c*) experimental pressure and (*d*) pressure difference

model is shown in Fig. 8(*a*). Numerical methods are used to study the parametric effect and to obtain variation rules on the cooling effect. Hence, the length of the plate is set to be 500 mm. The width changes from 60 mm to 140 mm for the study of the channel spacing effect and the thickness of the plate is chosen to be 2 mm. A cooling structure with a height and a width of 10 mm $\times$ 10 mm is installed beneath the plate, and a circular channel with a diameter of 5 mm is through the structure.

The mass flowrate of kerosene is in a range of 20–60 g/s, the inlet temperature varies from 300 to 400 K, and the outlet pressure is fixed as 3.0 MPa. A uniform heat flux of 5–15 kW/m^2 is loaded as the thermal boundary condition for the top surface of the plate. Details of the calculation conditions are shown in Table 4. The bottom surface of the plate structure is an adiabatic boundary condition. Other flow and thermal boundaries including symmetrical boundary conditions for plate sides and pressure outlet conditions for the channel outlet are shown in Fig. 8(*b*) as well as the mesh distribution.

3.2 Numerical Method and Meshes. For the coolant flow, Navier–Stokes equation is solved by using the differential volume method with the second-order upwind scheme for the convective term and the second-order central scheme for the viscous term. The renormalization group (RNG) k–ε model with enhanced wall treatment function is used for turbulence simulation. The semi-implicit method for pressure linked equation (SIMPLE) method is applied to solve the pressure–velocity coupling. The coupled heat transfer between the flow and solid domains is achieved by the continuity of temperature and heat flux across the fluid/solid interface.

The 3D meshes are divided into two domains: fluid domain and solid domain. The fluid domain consists of 0.77 million meshes and the solid domain consists of 0.6 million meshes, for a total of 1.37 million meshes. Structured meshes are used for the calculation of heat conduction in the plate. The fluid domain is divided into o-shaped meshes, and the size of the first grid layer from the wall is 0.01 mm, which meets the requirement of $\Delta y+\approx 1$. The mesh distribution is shown in Fig. 8(*b*).

In addition, grid independence is studied. The total mesh number of the fluid and solid domains is 0.46 million, 1.37 million, 3.00 million, and 5.09 million. The inlet fuel conditions are 20 g/s, 300 K, and 3.0 MPa and the wall heat flux is 5 kW/m^2, and the channel spacing of aluminum alloy is 100 mm. The top surface temperatures along the spanwise centerline are plotted and compared in Fig. 9. It can be seen from the figure that the results of meshes 1.37 million, 3.00 million, and 5.09 million are very close to each other, so the mesh 1.37 million is chosen for the present simulation.

3.3 Validation of the Numerical Method. To validate the present numerical method, the temperature distributions of experimental tests of Case A1 and Case A2 are calculated and the results are compared to the experimental data. The heat flux in the experiments is shown in Fig. 4, and it is in a range of 27.0–46.2 kW/m^2. However, the heat flux absorbed by the aluminum

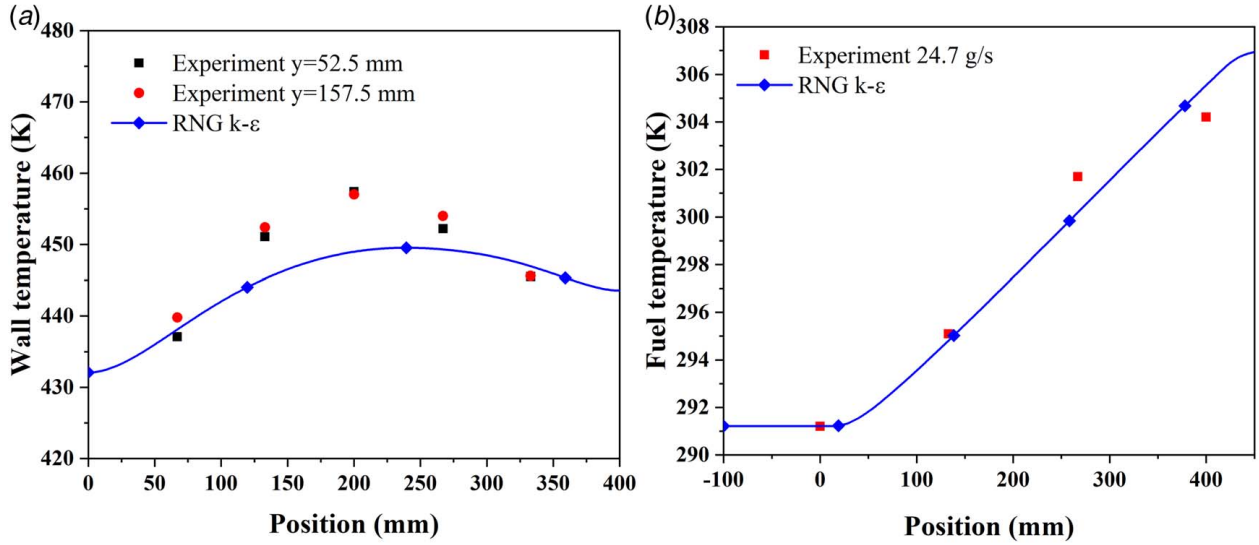

Fig. 6 Temperature distributions of Case A1: (*a*) surface temperature and (*b*) fuel temperature

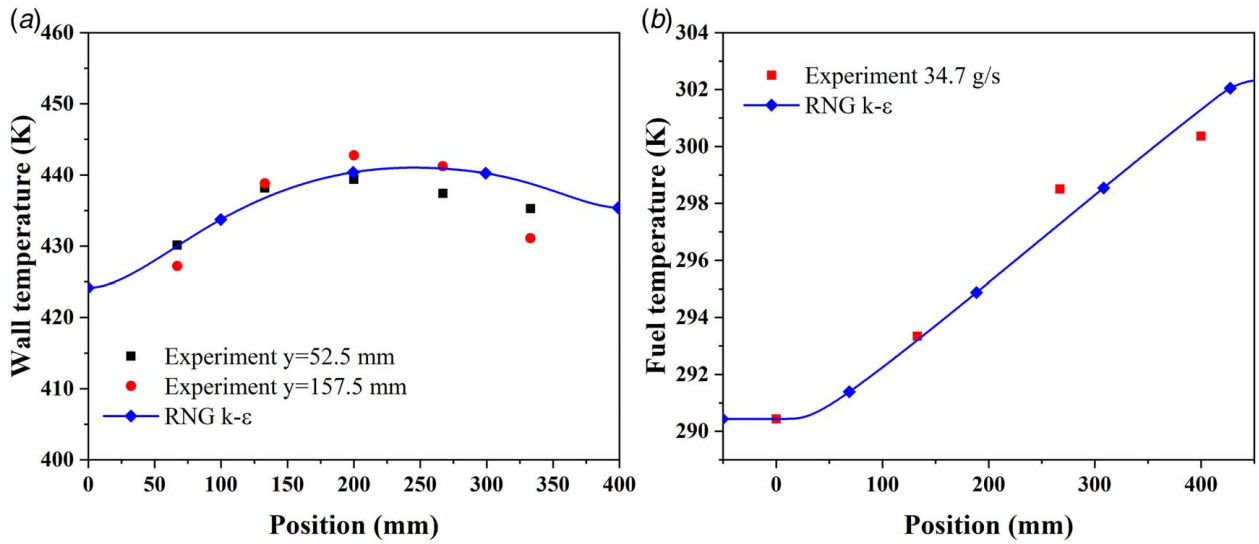

Fig. 7 Temperature distributions of Case A2: (*a*) surface temperature and (*b*) fuel temperature

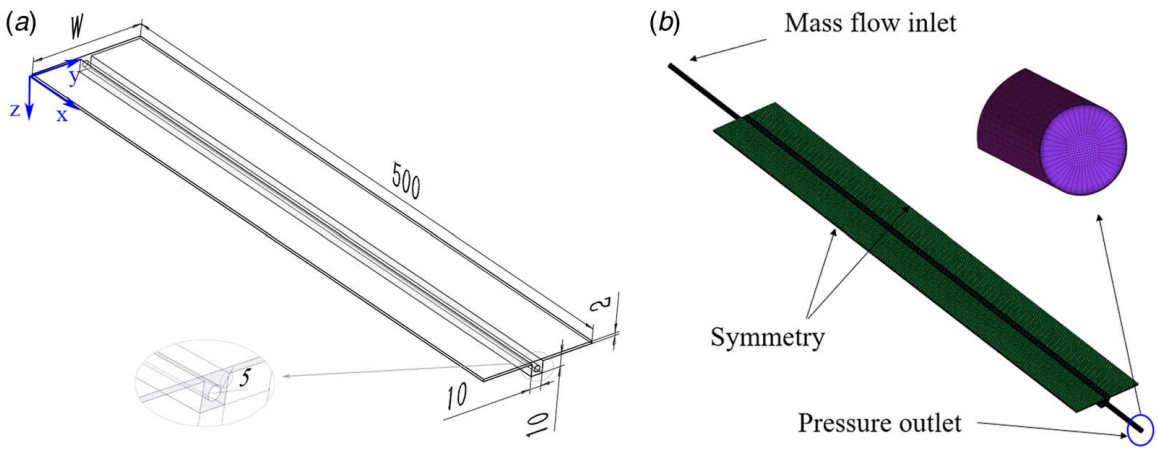

Fig. 8 Numerical model: (*a*) geometric configuration and (*b*) mesh distribution and boundary conditions

Table 4 The calculation parameters

Parameters	Value
Mass flowrate (g/s)	20, 30, 40, 50, 60
Heat flux (kW/m^2)	5, 8, 10, 12, 15
T_{in} (K)	300, 350, 400
W (mm)	60, 80, 100,120, 140

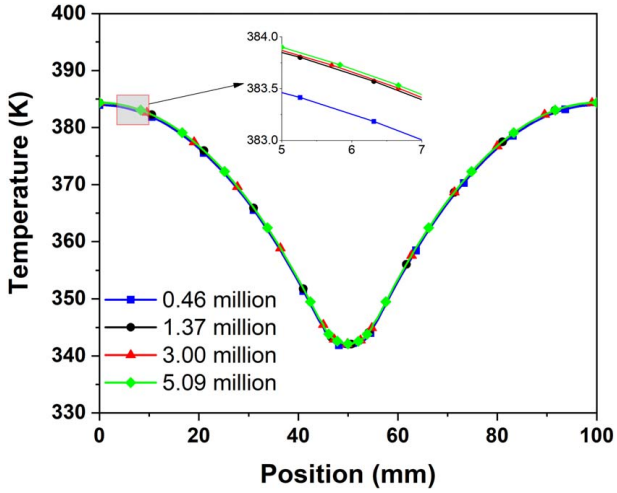

Fig. 9 Temperature distributions along the spanwise centerline with different meshes

alloy surface needs to be multiplied by the absorption rate (0.225), which is the thermal boundary condition for numerical validations. Figures 6 and 7 show the temperature comparisons of Case A1 and Case A2, respectively. It can be seen from the figures that the calculated results agree well with the experimental data. The root mean squared error (RMSE) of plate temperature for Case A1 and Case A2 is 5.1 K and 3.2 K, respectively, and the RMSE of kerosene temperature is 1.0 K and 0.8 K, respectively.

3.4 Data Analysis of the Numerical Results. Based on the numerical results, several important parameters indicating the heat transfer and flow resistance performance are obtained.

The temperature uniformity of the plate is expressed as follows:

$$\text{Uniformity} = \left(1 - \frac{T_{max} - T_{min}}{T_{avg}}\right) \times 100\% \tag{1}$$

where T_{min}, T_{avg}, and T_{max} are respectively the minimum temperature, the average temperature, and the maximum temperatures on the top surface of the plate.

The temperature difference is defined according to the literature [20]

$$\Delta T_{cf} = T_{channel} - T_f = T_{channel} - \frac{T_{in} + T_{out}}{2} \tag{2}$$

$$\Delta T_{af} = T_{avg} - T_f = T_{avg} - \frac{T_{in} + T_{out}}{2} \tag{3}$$

where ΔT_{cf} is the temperature difference between the inner wall of the channel and the coolant fluid. ΔT_{af} is the temperature difference between the plate surface and the coolant fluid. $T_{channel}$, T_f, and T_{in}, T_{out} are respectively the area-weighted average temperature of the inner wall of the channel, the arithmetic average temperature of inlet and outlet PR-3, the mass-weighted average inlet temperature, and the mass-weighted average outlet temperature.

Based on the principle of energy conservation, the heat transfer coefficient (HTC) is

$$\text{HTC} = \frac{q_{channel}}{\Delta T_{cf}} = \frac{q_w \times W \times L}{\pi \times d \times L \times \Delta T_{cf}} \tag{4}$$

where $q_{channel}$ is the circumferentially averaged heat flux of the circular cooling channel. q_w is the heat flux on the top surface of the plate. W is the channel spacing, L is the length of the plate, and d is the diameter of the cooling channel.

The overall heat transfer coefficient (OHTC) is

$$\text{OHTC} = \frac{q_w}{\Delta T_{af}} \tag{5}$$

It is worth noticing that HTC indicates the ability of convective heat transfer of coolant flow and OHTC shows the overall heat transferability of the plate including the convective heat transfer of coolant and the heat conduction of the structure.

The Biot number (Bi) is a dimensionless number that reflects the coupling effect of fluid–solid heat transfer. It is the ratio of the conductive thermal resistance to the convective thermal resistance. Its formula is as follows:

$$\text{Bi} = \frac{R_{Conductive}}{R_{Convective}} = \frac{R_{overall} - R_{Convective}}{R_{Convective}} = \frac{1/\text{OHTC} - 1/\text{HTC}}{1/\text{HTC}} \tag{6}$$

where $R_{overall}$ is the overall thermal resistance, $R_{conductive}$ is the conductive thermal resistance, and $R_{convective}$ is the convective thermal resistance. The smaller the Bi number, the more the uniform temperature of the solid structure.

The dimensionless flow resistance coefficient is calculated according to the following formula:

$$\xi = \frac{L}{d}\frac{2\Delta P}{\rho u^2} \tag{7}$$

where ΔP is the pressure difference between the inlet and the outlet, ρ is the density of kerosene, and u is the average velocity.

4 Numerical Results and Discussions

In this paper, the effects of fluid–solid coupling on the temperature distributions of 2a12 aluminum alloy plate and TA15 titanium alloy plate are numerically studied. The maximum temperature and temperature uniformity on the top surface of the plate are presented with varied channel spacing, heat flux, inlet temperature, and mass flowrate. In addition, the thermal resistance and flow resistance were also analyzed.

4.1 Temperature Distributions. The effects of channel spacing, heat flux, and inlet fuel temperature on the surface temperature distribution are studied. Figure 10 shows temperature contours of aluminum alloy structure at different channel spacing W with the same heat flux (5 kW/m^2) and kerosene mass flowrate (20 g/s). It can be seen from the figure that the maximum wall temperature is located at the edge and its value increases with the increase of channel spacing.

Figure 11 shows the contour of aluminum alloy surface temperature, fuel temperature, and velocity at a heat flux of 5 kW/m^2, W of 100 mm, and mass flowrate of 20 g/s. It is found that the temperature is low in the middle and high on both sides. The kerosene temperature and velocity in the cooling channel indicate a fully developed channel flow except for a short region near the inlet.

Figure 12 shows the maximum surface temperature and temperature uniformity at channel spacing increasing from 60 mm to 140 mm for two materials and two fuel mass flowrates. With the increase of the channel spacing, the maximum surface temperature of the actively cooled plates increases, and the temperature uniformity decreases. It can be seen from Fig. 12 that the maximum temperature of the titanium alloy plate is significantly higher than that

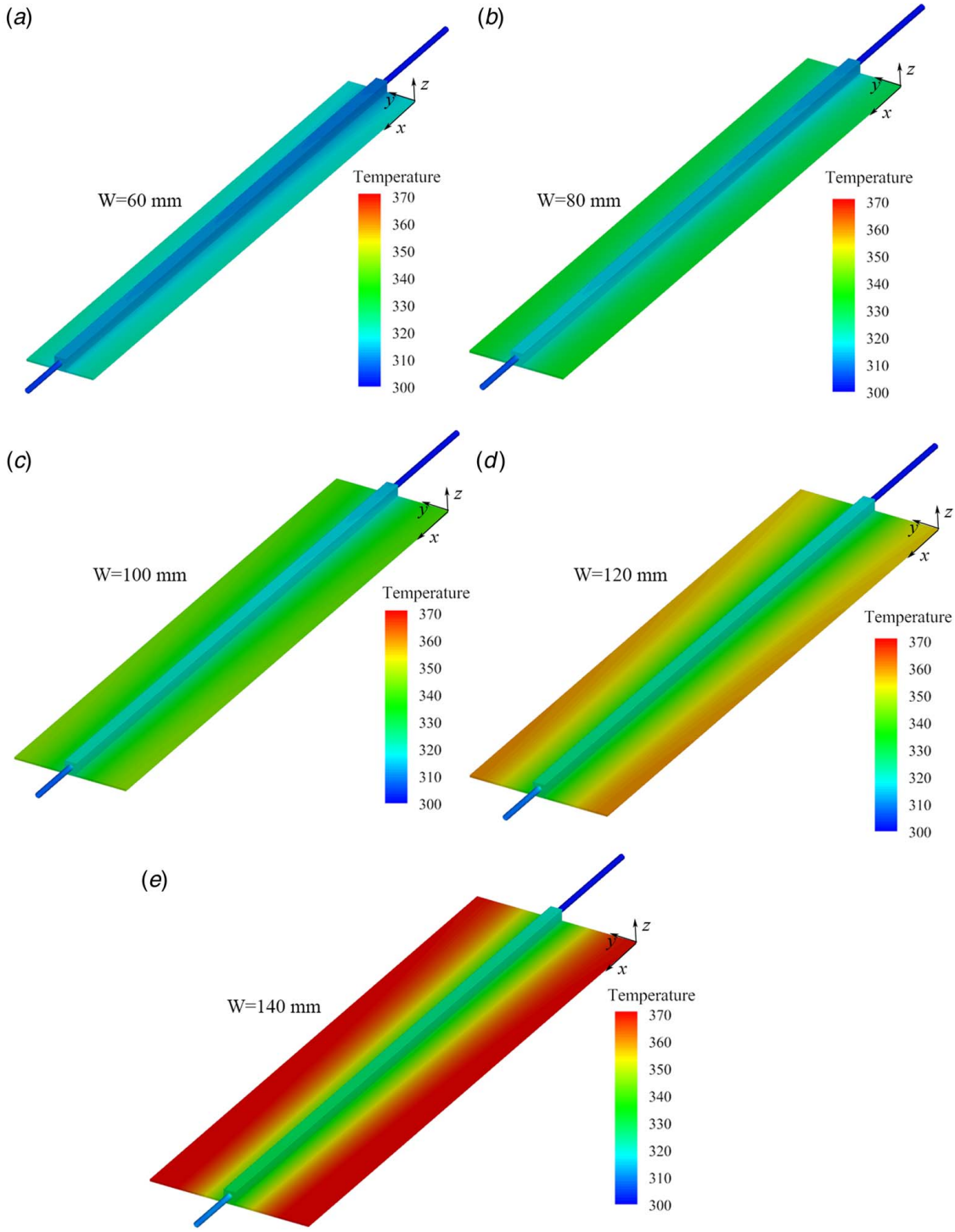

Fig. 10 Temperature contours of the aluminum alloy plate with different channel spacing: (*a*) $W = 60$ mm, (*b*) $W = 80$ mm, (c) $W = 100$ mm, (*d*) $W = 120$ mm, and (e) $W = 140$ mm

of the aluminum alloy plate. The increased rate of titanium alloy as a function of channel spacing is also larger than that of aluminum alloy. This is because with smaller thermal conductivity, the overall cooling effectiveness is lower and the effect of channel spacing is more obvious. The temperature uniformity of aluminum alloys is significantly higher than that of titanium alloys. Moreover, increasing the mass flowrate reduces the maximum temperature slightly for both alloys. When the channel spacing is 140 mm, as the coolant mass flowrate increases from 20 g/s to 60 g/s, the maximum temperature of aluminum alloy is reduced by 16.9 K, accounting for 16.4% of the maximum temperature, while the maximum temperature of titanium alloy is reduced by 12.9 K, accounting for 2.3% of the maximum temperature. It can be found that titanium alloy is less sensitive to the mass flowrate of the cooling medium than aluminum alloy.

The effect of heat flux on the surface temperature is shown in Fig. 13. It can be seen from Fig. 13 that the maximum temperature increases almost linearly with the heat flux. When the mass flowrate is 20 g/s and the heat flux increases from 5 kW/m^2 to 15 kW/m^2, the maximum temperature of the titanium alloy increases by 212.8 K, and the uniformity decreases by 23.7%. Similarly, the maximum temperature of the titanium alloy increases by 417.3 K, and the

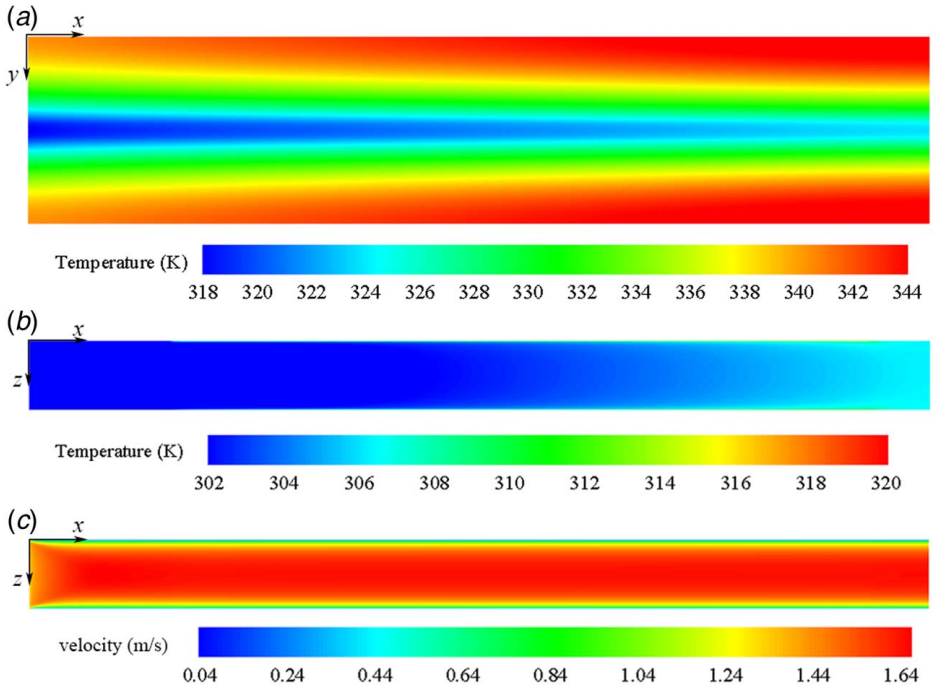

Fig. 11 Distribution diagram at 20 g/s: (*a*) surface temperature, (*b*) RP-3 temperature, and (c) velocity

uniformity decreases by 45.6%. The figure shows that the maximum temperature and temperature uniformity are considerably affected by the heat flux.

The influence of inlet temperature on the surface temperature of aluminum alloy plate is shown in Fig. 14 when the flowrate is 20 g/s and the heat flux is 5 kW/m^2. It can be seen that as the inlet temperature is higher, the maximum temperature is larger. Moreover, the temperature uniformity is higher as well. The better uniformity attributes to the larger thermal conductivity of aluminum alloy at higher temperatures and to the more efficient heat transfer of kerosene flow at higher temperatures.

4.2 Analysis of Thermal Resistance. The active cooling plate structure is fluid–structure coupled heat transfer. The overall thermal resistance includes the convective thermal resistance in the cooling channel and the conductive thermal resistance of the solid structure. The Biot number (Bi) is the ratio of the conductive thermal resistance to the convective thermal resistance, which is calculated by formula (6).

The changes of convective HTC of kerosene flow and the OHTC of the cooling plate are studied with varied fuel mass flowrate, channel spacing, and material. Figures 15(*a*) and 15(*b*) show the change of HTC and OHTC as a function of channel spacing with different mass flowrates. The surface heat flux is kept at the same value of 5 kW/m^2. It can be seen from Fig. 15(*a*) that HTC is mainly affected by mass flow, and it is very weakly related to the channel spacing. However, as shown in Fig. 15(*b*), OHTC is affected strongly by material, channel spacing, and mass flowrate. As the channel spacing increases, the OHTC decreases considerably due to the lower thermal conductivity of the plate with a larger width. Since OHTC represent the overall cooling performance of

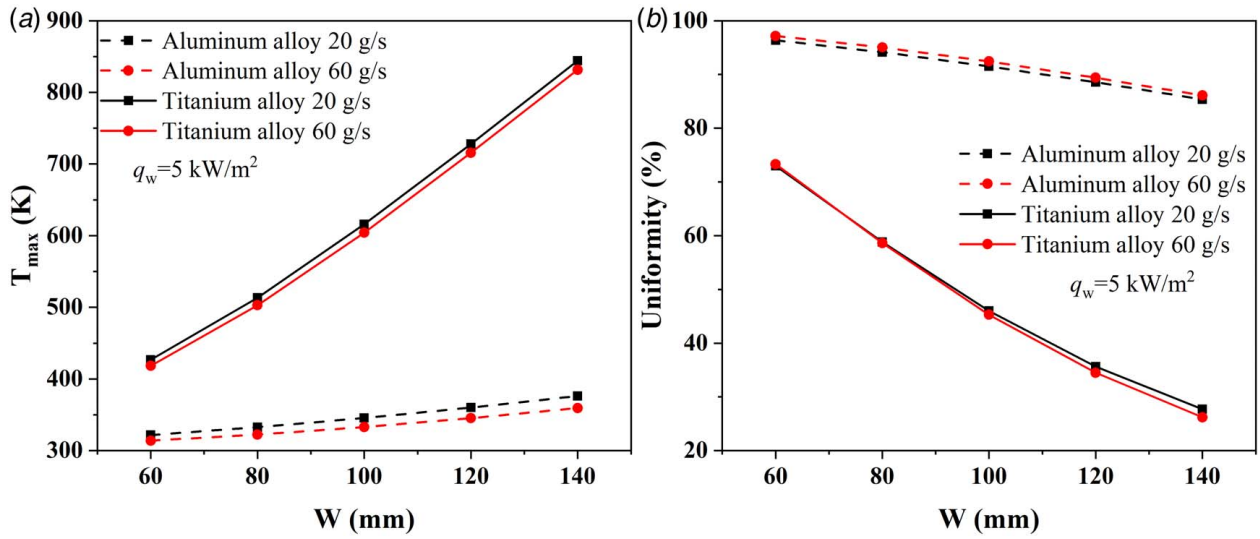

Fig. 12 Maximum surface temperature and temperature uniformity as functions of channel spacing and fuel mass flowrate: (*a*) maximum temperature and (*b*) uniformity

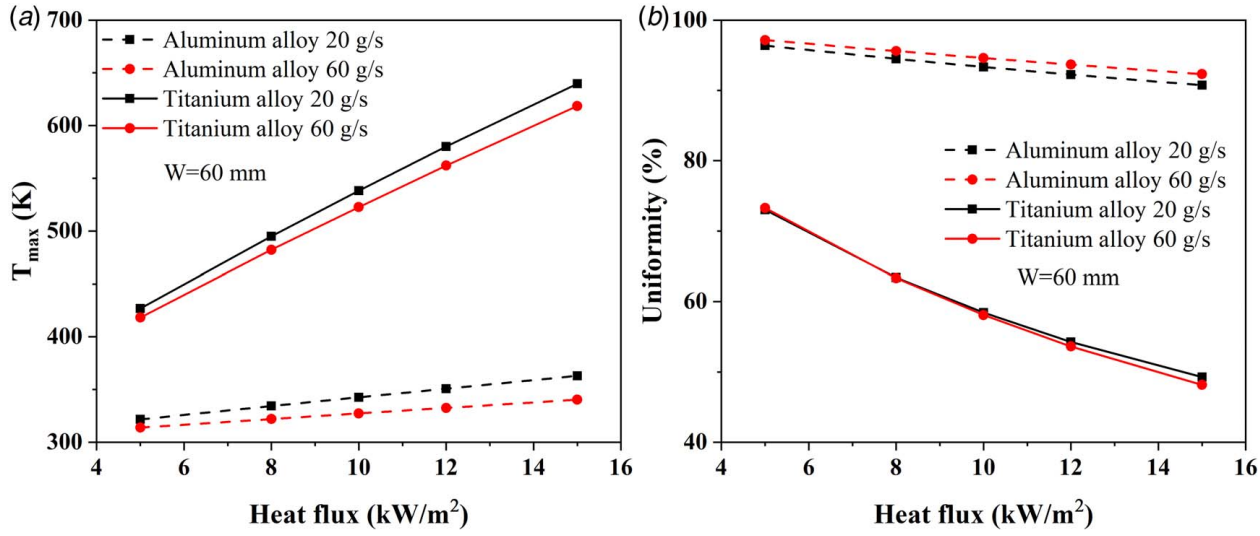

Fig. 13 Maximum surface temperature and temperature uniformity as functions of heat flux and fuel mass flowrate: (*a*) maximum temperature and (*b*) uniformity

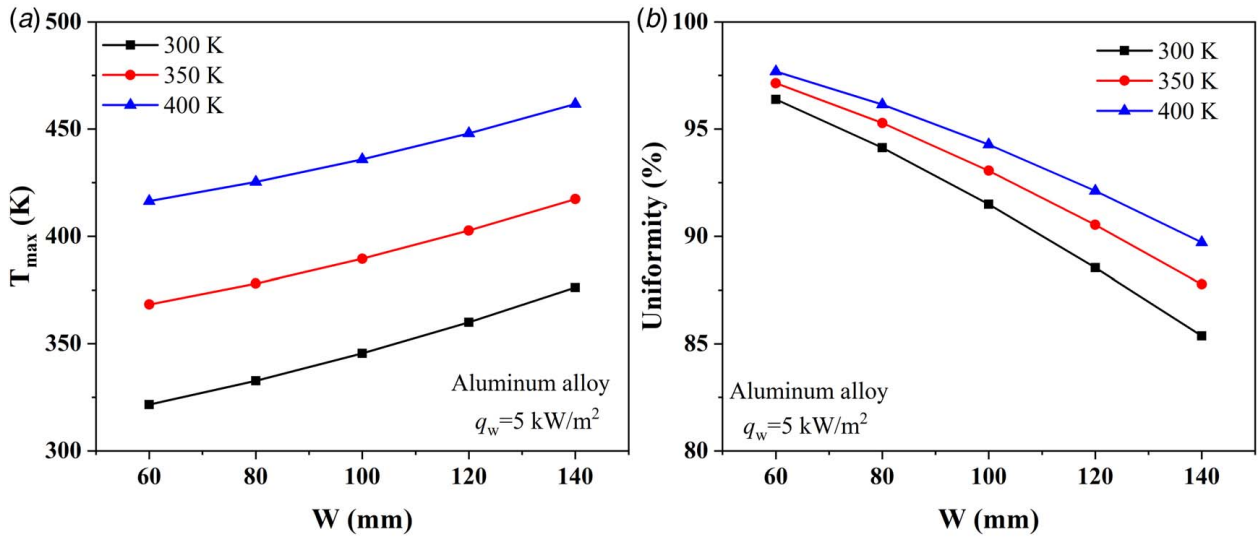

Fig. 14 The influence of inlet temperature on aluminum alloy plates: (*a*) maximum temperature and (*b*) uniformity

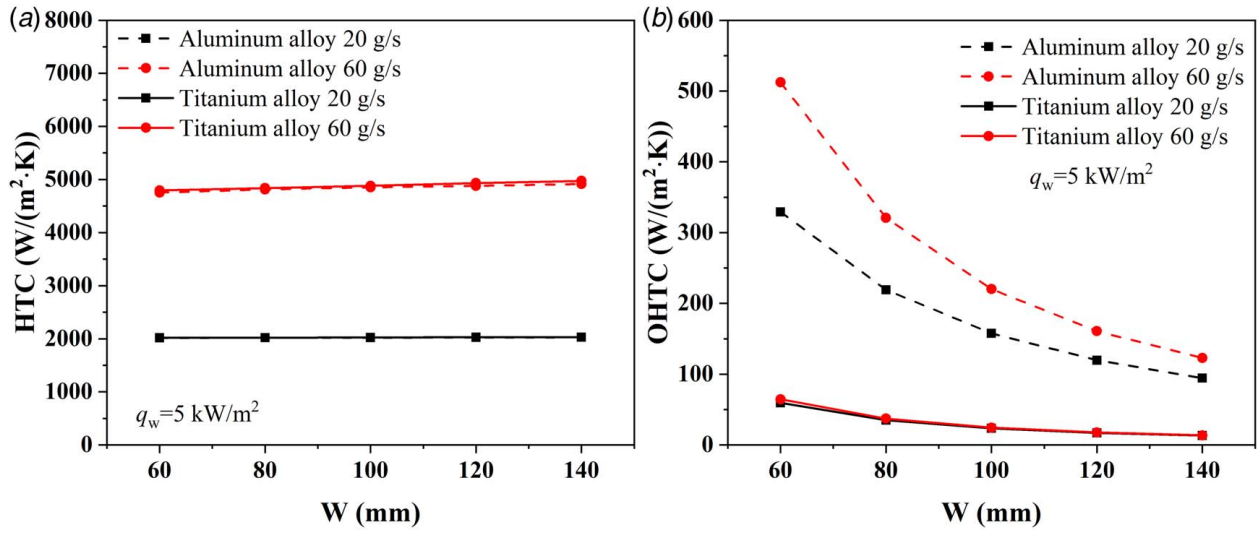

Fig. 15 (*a*) HTC and (*b*) OHTC changes with mass flow, material, and channel spacing

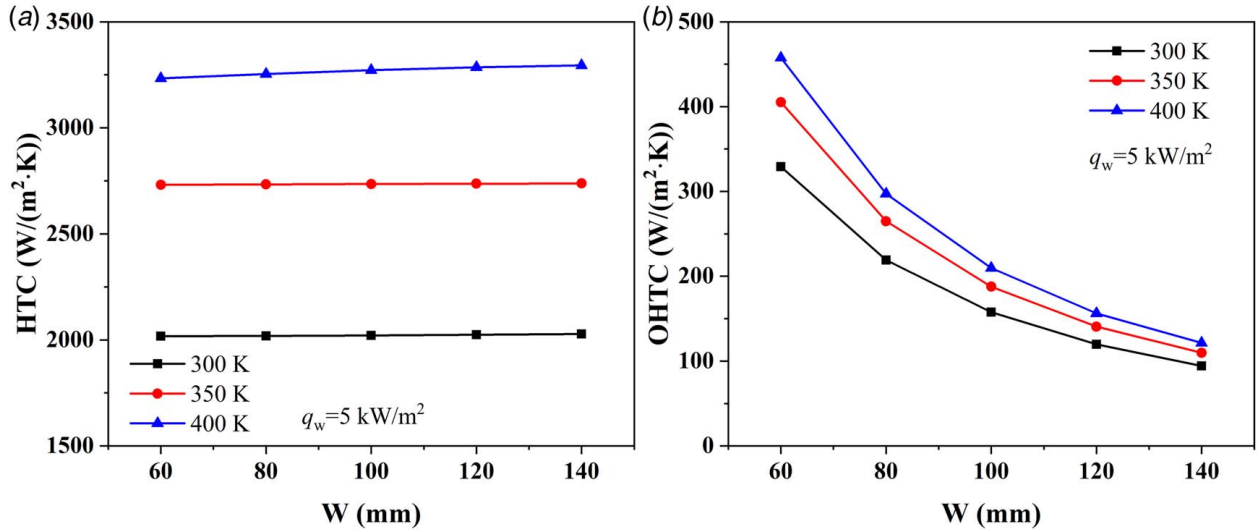

Fig. 16 (*a*) HTC and (*b*) OHTC changes with inlet temperature and channel spacing

the plate with cooling, its reduction indicates lower overall cooling efficiency. Moreover, the OHTC of aluminum alloy plate is much higher than that of titanium alloy plate since the thermal conductivity of aluminum alloy is large, so thermal resistance across the plate is relatively small. The OHTC values for the two materials also explain that under the same flow and heat conditions, the maximum temperature of aluminum alloy is much lower than that of titanium alloy, and the temperature uniformity of aluminum alloy is much higher. The effect of inlet temperature on HTC and OHTC of the aluminum alloy at a heat flux of 5 kW/m^2 is shown in Fig. 16. It can be seen that as inlet temperature increases, the HTC has a significant increase; however, the increase of OHTC with inlet temperature is smaller.

When the mass flowrate is 60 g/s and the heat flux is 5 kW/m^2, the change of thermal resistance of aluminum alloy and titanium alloy with channel spacing is shown in Fig. 17. The overall thermal resistance consists of two parts: one is the conductive thermal resistance and another is convective thermal resistance, as shown in formula (6). It can be seen from the figure that the overall thermal resistance is mainly composed of the conductive thermal resistance. When W is 60 mm, the conductive thermal resistance of the aluminum alloy plate accounts for 89.2% of the total thermal resistance, and the conductive thermal resistance of the titanium alloy plate accounts for 98.6%. Moreover, the conductive thermal resistance of titanium alloy is significantly higher than that of aluminum alloy. The conductive thermal resistance of the aluminum alloy is 0.0017–0.0079 m^2·K/W, and that of titanium alloy is 0.015–0.073 m^2·K /W.

Figure 18 shows the variation of Biot number (Bi) with channel spacing for aluminum alloy and titanium alloy plates. The smaller the Bi number, the more the uniform temperature distribution of the solid structure. It can be seen from the figure that the Bi number of titanium alloy is significantly higher than that of aluminum alloy. At 20 g/s, the Bi number of titanium alloys ranges from 32 to 153, while that of aluminum alloys ranges from 5 to 21. It explains that the temperature uniformity of aluminum alloy plate is much better than at of titanium alloy plate under the same cooling conditions.

4.3 Analysis of Flow Resistance. The pressure difference in the active cooling system is another important factor that needs to be considered. When the mass flowrate is 20 g/s and heat flux is 5 kW/m^2, the influences of channel spacing and inlet temperature on the pressure difference are shown in Fig. 19(*a*). It can be seen that as the inlet temperature and channel spacing increase, the

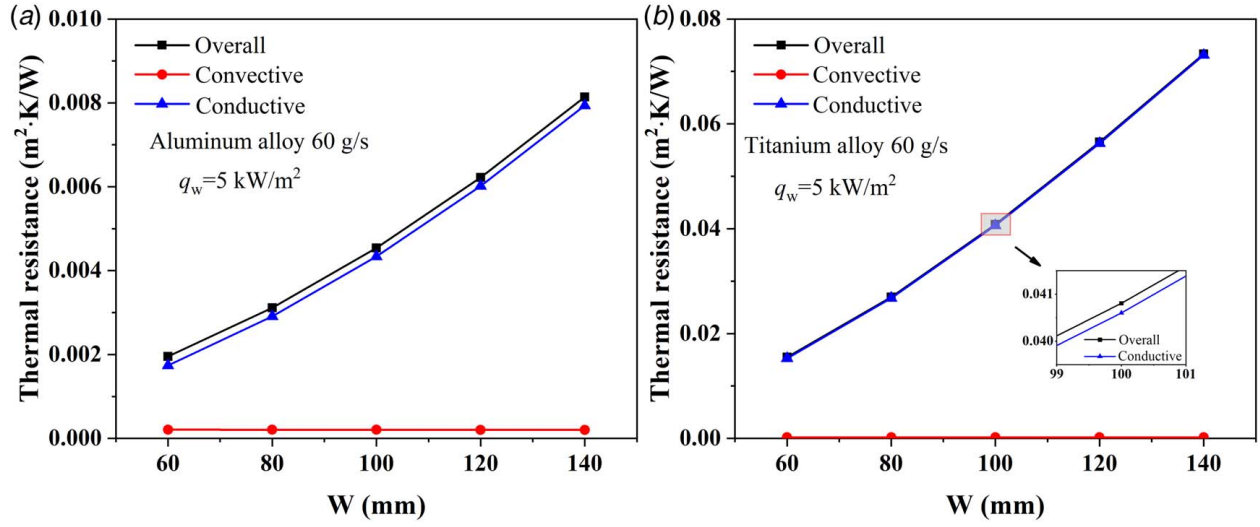

Fig. 17 Thermal resistance changes with channel spacing: (*a*) aluminum alloy and (*b*) titanium alloy

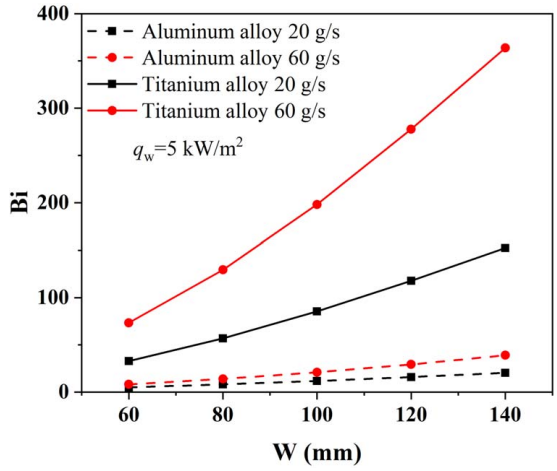

Fig. 18 Biot number changes with the channel spacing

pressure difference decreases. Although the increase of inlet temperature leads to the increase of fluid velocity, which is beneficial to the increase of fluid resistance, it also causes the viscosity of the RP-3 to decrease, resulting in a decrease in the resistance coefficient, which is the main factor for the decrease of pressure difference, as shown in Fig. 20. When the inlet temperature of aluminum alloy plates is fixed as 300 K, the influences of mass flowrate and heat flux on the pressure difference are shown in Fig. 19(*b*). It can be seen from the figure that as the mass flowrate increases, the pressure difference increases significantly. As the heat flux increases, the pressure difference slightly decreases. This is because the fuel temperature is higher at high heat flux. For the present test cases, the pressure drop through the cooling channel is found to be quite small with a maximum value of 18.8 kPa.

The dimensionless flow resistance coefficient ξ varies with channel spacing and mass flowrate as shown in Fig. 20. It can be seen from the figure that the flow resistance coefficient is smaller at higher fuel inlet temperature, and it decreases gradually as the mass flowrate increases.

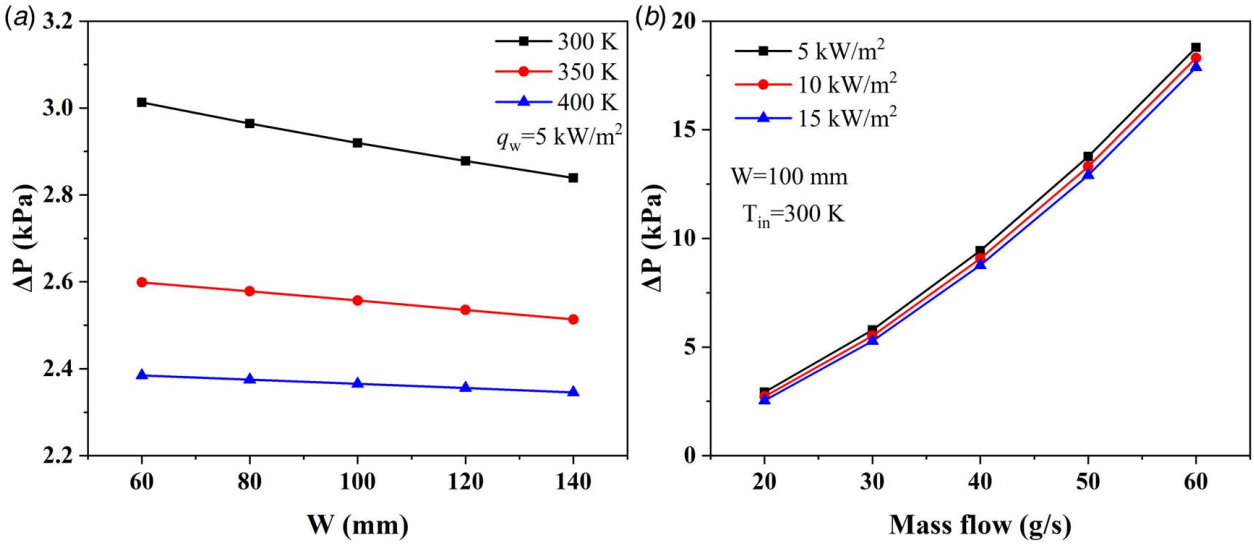

Fig. 19 Pressure difference of aluminum alloy plates: (*a*) channel spacing and (*b*) mass flow

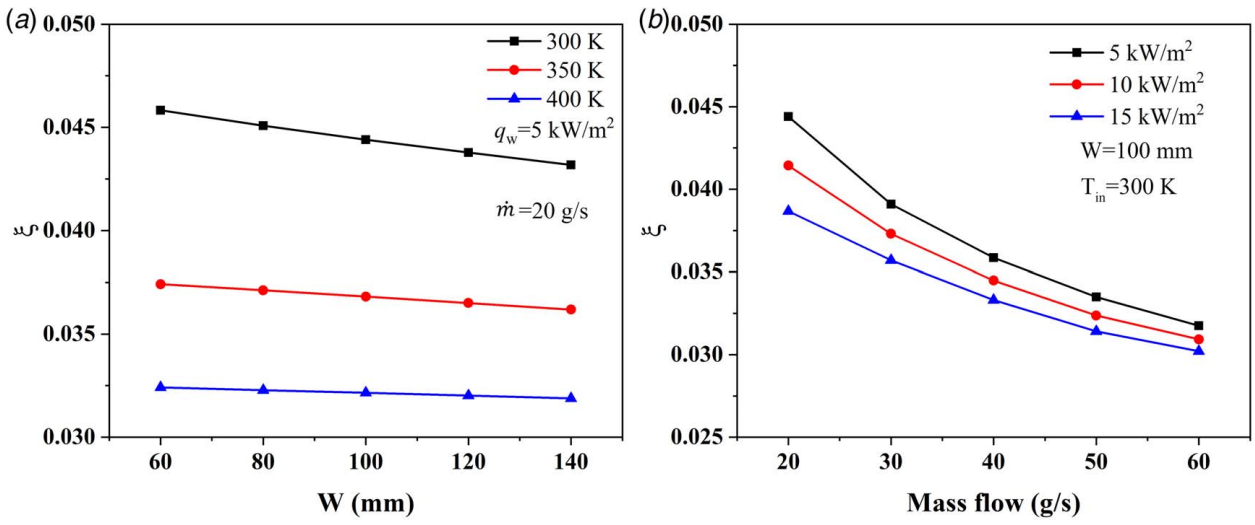

Fig. 20 Flow resistance coefficient varies with channel spacing and mass flow: (*a*) channel spacing and (*b*) mass flow

5 Conclusions

In this paper, the effects of channel spacing, heat flux, mass flowrate, and inlet temperature on temperature distributions of 2a12-type aluminum alloy and TA15-type titanium alloy plates with kerosene cooling are studied through experimental and numerical methods. The thermal resistance and flow resistance were also analyzed. The following conclusions are derived from the present work.

(1) The maximum temperature and temperature uniformity are mainly affected by the channel spacing and the heat flux. The Biot number of titanium alloy plate is significantly larger than that of aluminum alloy plate, indicating that the temperature distribution of aluminum alloy plate is more uniform.
(2) Increasing the mass flow from 20 g/s to 60 g/s can reduce the plate surface temperature by 12.9–16.9 K, accounting for 16.4% of aluminum alloys and 2.3% of titanium alloys. The aluminum alloy plate is more likely to be affected by the mass flowrate than the titanium alloy plate.
(3) The conductive thermal resistance accounts for more than 89% of the overall thermal resistance for both materials. The conductive thermal resistance of the aluminum alloy plate is 0.0017–0.0079 m^2 K/W, while the conductive thermal resistance of the titanium alloy plate is 0.015–0.073 m^2 K/W. In addition, the change of HTC is mainly affected by kerosene mass flowrate and inlet temperature, while the OHTC is determined by material, kerosene mass flowrate, and channel spacing.
(4) Reducing the channel spacing, increasing the mass flowrate, and increasing the inlet temperature can improve the surface temperature uniformity. In addition, as the mass flowrate increases, the differential pressure increases, while the flow resistance coefficient decreases.

Conflict of Interest

There are no conflicts of interest.

Data Availability Statement

The authors attest that all data for this study are included in the paper.

Nomenclature

d = diameter, m
q = heat flux, W/m^2
$\dot{m}$ = mass flowrate, kg/s
L = length of plate, m
R = Thermal resistance, m^2 K/W
T = temperature, K
W = width of plate/channel spacing, m
T_{ij} = surface temperature of (i,j) position, K
ΔP = pressure difference, Pa
ΔT = temperature difference, K

Subscripts

f = fluid
in = inlet
avg = average
max = maximum
min = minimum
out = outlet
channel = channel wall

References

[1] Youn, B., and Mills, A. F., 1995, "Cooling Panel Optimization for the Active Cooling System of a Hypersonic Aircraft," J. Thermophys. Heat Trans., **9**(1), pp. 136–143.
[2] Wang, N., Zhou, J., Pan, Y., and Wang, H., 2014, "Experimental Investigation on Flow Patterns of RP-3 Kerosene Under Sub-Critical and Supercritical Pressures," Acta Astronaut., **94**(2), pp. 834–842.
[3] Li, X. F., Huai, X. L., Cai, J., Zhong, F. Q., Fan, X. J., and Guo, Z. X., 2011, "Convective Heat Transfer Characteristics of China RP-3 Aviation Kerosene at Supercritical Pressure," Appl. Therm. Eng., **31**(14–15), pp. 2360–2366.
[4] Ulas, A., and Boysan, E., 2013, "Numerical Analysis of Regenerative Cooling in Liquid Propellant Rocket Engines," Aerosp. Sci. Technol., **24**(1), pp. 187–197.
[5] Chen, Y., Wang, Y., Bao, Z. W., Zhang, Q. Y., and Li, X. Y., 2016, "Numerical Investigation of Flow Distribution and Heat Transfer of Hydrocarbon Fuel in Regenerative Cooling Panel," Appl. Therm. Eng., **98**, pp. 628–635.
[6] Sun, X., Meng, H., and Zheng, Y., 2019, "Asymmetric Heating and Buoyancy Effects on Heat Transfer of Hydrocarbon Fuel in a Horizontal Square Channel at Supercritical Pressures," Aerosp. Sci. Technol., **93**, p. 105358.
[7] Taddeo, L., Gascoin, N., Chetehouna, K., Ingenito, A., Stella, F., Bouchez, M., and Le Naour, B., 2017, "Experimental Study of Pyrolysis–Combustion Coupling in a Regeneratively Cooled Combustor: System Dynamics Analysis," Aerosp. Sci. Technol., **67**, pp. 473–483.
[8] Wang, J. X., Li, Y. Z., Liu, X. D., Shen, C. Q., Zhang, H. S., and Xiong, K., 2021, "Recent Active Thermal Management Technologies for the Development of Energy-Optimized Aerospace Vehicles in China," Chin. J. Aeronaut., **34**(2), pp. 1–27.
[9] Nižetić, S., Giama, E., and Papadopoulos, A. M., 2018, "Comprehensive Analysis and General Economic-Environmental Evaluation of Cooling Techniques for Photovoltaic Panels, Part II: Active Cooling Techniques," Energy Convers. Manag., **155**, pp. 301–323.
[10] Dong, J., Zhuang, X. R., Xu, X. H., Miao, Z. H., and Xu, B., 2018, "Numerical Analysis of a Multi-Channel Active Cooling System for Densely Packed Concentrating Photovoltaic Cells," Energy Convers. Manag., **161**, pp. 172–181.
[11] Li, Y., Xie, G. N., and Sunden, B., 2020, "Flow and Thermal Performance of Supercritical n-Decane in Double-Layer Channels for Regenerative Cooling of a Scramjet Combustor," Appl. Therm. Eng., **180**, p. 115695.
[12] Wang, H. J., Luo, Y. S., Gu, H. F., Li, H. Z., Chen, T. K., Chen, J. H., and Wu, H. B., 2012, "Experimental Investigation on Heat Transfer and Pressure Drop of Kerosene at Supercritical Pressure in Square and Circular Tube With Artificial Roughness," Exp. Therm. Fluid Sci., **42**, pp. 16–24.
[13] Dang, G. X., Zhong, F. Q., Zhang, Y. J., and Zhang, X. Y., 2015, "Numerical Study of Heat Transfer Deterioration of Turbulent Supercritical Kerosene Flow in Heated Circular Tube," Int. J. Heat Mass Transfer, **85**, pp. 1003–1011.
[14] Jing, T. T., He, G. Q., Qin, F., Li, W. Q., Zhang, D., and Zhang, P. K., 2018, "An Innovative Self-adaptive Method for Improving Heat Sink Utilization Efficiency of Hydrocarbon Fuel in Regenerative Thermal Protection System of Combined Cycle Engine," Energy Convers. Manag., **178**, pp. 369–382.
[15] Xu, K. K., Tang, L. J., and Meng, H., 2015, "Numerical Study of Supercritical-Pressure Fluid Flows and Heat Transfer of Methane in Ribbed Cooling Tubes," Int. J. Heat Mass Transfer, **84**, pp. 346–358.
[16] Zhao, B. F., Xie, L. Y., Wang, L., Hu, Z. Y., Zhou, S., and Bai, X., 2021, "A New Multiaxial Fatigue Life Prediction Model for Aircraft Aluminum Alloy," Int. J. Fatigue, **143**, p. 105993.
[17] Rahman, M., Wang, Z. G., and Wong, Y. S., 2006, "A Review on High-Speed Machining of Titanium Alloys," JSME Int. J. C-Mech. Sys., **49**(1), pp. 11–20.
[18] Yan, M. G., Liu, B. C., and Li, J. G., 2001, *China Aeronautical Materials Handbook*, Standards Press of China, China.
[19] Zhong, F. Q., Fan, X. J., Yu, G., Li, J. G., and Sung, C. J., 2009, "Heat Transfer of Aviation Kerosene at Supercritical Conditions," J. Thermophys. Heat Trans., **23**(3), pp. 543–550.
[20] Yang, S. M., and Tao, W. Q., 2006, *Heat Transfer*, Higher Education Press, China.